nature COMMUNICATIONS

ARTICLE

https://doi.org/10.1038/s41467-020-17584-9 OPEN

Scalable neutral H_2O_2 electrosynthesis by platinum diphosphide nanocrystals by regulating oxygen reduction reaction pathways

Hui Li[1,8], Peng Wen[2,8], Dominique S. Itanze[1], Zachary D. Hood[3,4], Shiba Adhikari[5], Chang Lu[1], Xiao Ma[1], Chaochao Dun[6], Lin Jiang[7], David L. Carroll[6], Yejun Qiu[2]✉ & Scott M. Geyer[1]✉

Despite progress in small scale electrocatalytic production of hydrogen peroxide (H_2O_2) using a rotating ring-disk electrode, further work is needed to develop a non-toxic, selective, and stable O_2-to-H_2O_2 electrocatalyst for realizing continuous on-site production of neutral hydrogen peroxide. We report ultrasmall and monodisperse colloidal PtP_2 nanocrystals that achieve H_2O_2 production at near zero-overpotential with near unity H_2O_2 selectivity at 0.27 V vs. RHE. Density functional theory calculations indicate that P promotes hydrogenation of OOH* to H_2O_2 by weakening the Pt-OOH* bond and suppressing the dissociative OOH* to O* pathway. Atomic layer deposition of Al_2O_3 prevents NC aggregation and enables application in a polymer electrolyte membrane fuel cell (PEMFC) with a maximum r(H_2O_2) of 2.26 mmol h^{-1} cm^{-2} and a current efficiency of 78.8% even at a high current density of 150 mA cm^{-2}. Catalyst stability enables an accumulated neutral H_2O_2 concentration in 600 mL of 3.0 wt% (pH = 6.6).

[1] Department of Chemistry, Wake Forest University, Winston-Salem, NC 27106, USA. [2] Shenzhen Engineering Lab of Flexible Transparent Conductive Films, School of Materials Science and Engineering, Harbin Institute of Technology, Shenzhen 518055, China. [3] Center for Nanophase Materials Sciences (CNMS), Oak Ridge National Laboratory (ORNL), Oak Ridge, TN 37831, USA. [4] Department of Materials Science and Engineering, Massachusetts Institute of Technology, Cambridge, MA 02139, USA. [5] Material Science and Technology Division (MSTD), Oak Ridge National Laboratory (ORNL), Oak Ridge, TN 37831, USA. [6] Center for Nanotechnology and Molecular Materials, Department of Physics, Wake Forest University, Winston-Salem, NC 27109, USA. [7] Institute of Functional Nano and Soft Materials (FUNSOM), Soochow University, Suzhou, Jiangsu 215123, China. [8] These authors contributed equally: Hui Li, Peng Wen. ✉email: yejunqiu@hit.edu.cn; geyersm@wfu.edu

Hydrogen peroxide (H_2O_2) is a valuable chemical for a variety of industrial applications, as well as a potential energy carrier alternative to oil or hydrogen in fuel cells. H_2O_2 is currently manufactured by a large-scale indirect anthraquinone process and the under-developed direct synthesis from a H_2 and O_2 mixture[1]. The anthraquinone process involves multiple redox reaction steps and requires expensive palladium-based hydrogenation catalysts. Furthermore, energy-intensive distillation for obtaining high concentration H_2O_2 is necessary to minimize transportation and storage costs. Direct synthesis via H_2 and O_2 is more straightforward but potentially explosive. Electrochemical H_2O_2 production through the oxygen reduction reaction (ORR) in an electrolyzer or fuel cell is an attractive and cost-effective route due to its mild operation conditions, on-site production, and tunable concentration[2]. However, it is still a great challenge to develop efficient and stable electrocatalysts that are selective toward the two-electron ORR.

Incorporation of an efficient and stable catalyst into a proton-exchange membrane electrolyzer or fuel cell is a promising route to commercialization. Many potential ORR electrocatalysts, mainly including carbon-based materials and noble metal-based materials, have been reported for H_2O_2 production in alkaline or acidic electrolyte[3]. Carbon-based electrocatalysts typically perform well in alkaline solution but show low intrinsic activity and stability in acidic media[4]. Bimetallic noble metal alloys, such as Au–Pd, Pt–Hg, Pd–Hg, and Au–Pt–Ni, catalyze ORR through two-electron pathways with selectivity as high as 95%[5–7]. The goal of secondary metal incorporation is to change the electronic structure of the primary catalytic site and optimize the binding strength of reaction intermediates[8]. An ideal two-electron ORR electrocatalyst should possess a suitable binding strength for OOH* (not too strong or too weak) and suppress the O–O bond breakage in OOH* to O*. However, stability of the bimetallic alloys is a concern, particularly for medicinal or water treatment applications. Elemental leaching hinders the long-term ORR stability and the leached ingredient (particularly toxic Hg) devalues the H_2O_2 product and increases the separation cost[9,10]. Apart from the metal alloying strategy, incorporation of non-metal elements such as phosphorus, sulfur, and boron into metals to form multicomponent alloys has been demonstrated to be an attractive and effective way to improve the electrocatalytic activity of metal catalysts[11–15]. Particularly, our previous work found that electronegative phosphorus (P) was able to regulate the binding strength of intermediates in ORR and improve the four-electron ORR activity for cobalt phosphide[16]. Since Pt is the most widely used material for four-electron ORR, it is highly desirable to investigate if P alloying is able to alter the electronic structure of P-rich platinum phosphide and shift the reaction pathway from a four-electron to a two-electron pathway.

Ultrasmall nanoparticle catalysts not only have a high surface to volume ratio which reduces cost for precious metal catalysts by increasing the per mass surface area, but also lead to higher exposure of low-coordinated edge sites for improved electrocatalytic activity[17]. However, small nanoparticle electrocatalysts are prone to aggregation during long-term electrochemical operation, which lowers surface area, reduces available active sites and consequently causes electrocatalytic activity degradation[18]. Encapsulation of nanoparticles in a porous ultrathin shell of a stable metal oxide can largely preserve the catalytic activity while increasing the resistance against aggregation[19]. Atomic layer deposition (ALD), a thin-film deposition technique that allows growth of conformal coating through a self-limiting vapor growth process, has been employed to deposit ultrathin metal oxide layers to overcoat and stabilize nanoparticle catalysts for optimizing both activity and durability[20–22]. Therefore, ALD is of interest to prevent aggregation of ultrasmall platinum phosphide nanocrystals and preserve their ORR activity and selectivity during long-term electrocatalysis.

Generally, the ORR activity of an electrocatalyst is initially evaluated by the rotating-ring disk electrode (RRDE) technique, which provides only an upper limit to the activity and selectivity of two-electron ORR due to rapid transportation of H_2O_2 from disk to ring[2]. In real devices, such as those based on a membrane electrode assembly (MEA) architecture, additional transport factors must be considered. These include the slow diffusion rate of H_2O_2 from the catalyst and gas diffusion layers to the output stream and the chance for further H_2O_2 reduction or chemical decomposition[23]. Yamanaka and Wilkinson's groups have reported MEA-based water electrolyzers and fuel cell reactors for production of small amounts of neutral H_2O_2 by continuously feeding gaseous O_2 into the cathodic chamber[24–27]. However, the long-term stability for efficient O_2-to-H_2O_2 production at high current levels is still a large challenge due to the severe H_2O_2 accumulation at the interface between ORR catalyst layer and proton-exchange membrane, particularly if there is no solvent flow to remove the concentrated product. To reach a high concentration at a large scale will require incorporation of an efficient two-electron ORR catalyst into a system with sufficient long-term stability in the presence of high H_2O_2 content to allow for continuous recycling of the H_2O_2 product to reach medical level concentrations.

Herein, monodisperse colloidal platinum diphosphide nanocrystals (PtP_2 NCs) with an uniform size of 3 nm are directly synthesized by a hot-injection method using platinum(II) 2,4-pentanedionate and tris(trimethylsilyl)phosphine. Unlike ORR catalyzed by Pt NCs which follow a conventional four-electron pathway, the ultrasmall PtP_2 NCs proceed through a two-electron pathway with a nearly zero overpotential to initialize the O_2-to-H_2O_2 reaction and achieve a maximum selectivity of 98.5% at 0.27 V vs. RHE. DFT calculations reveal that changes in electron density and increased Pt atom separation due to P incorporation leads to a weaker adsorption of the key OOH* intermediate and inhibition of subsequent O–O breakage of OOH* to form the O* intermediate. The ultrasmall PtP_2 NCs are treated by ALD of an alumina overcoat and post-annealing to suppress aggregation and maintain electrocatalytic stability. The resulting catalyst is employed in a PEMFC to achieve a steady neutral H_2O_2 formation rate of 2.26 mmol h^{-1} cm^{-2} and the accumulated H_2O_2 concentration reaches 3 wt% in 65 h and as high as 1.21 M in 600 mL after continuous cycling for 120 h.

Results

Synthesis and characterization. To synthesize ultrasmall and highly monodisperse platinum phosphide NCs, platinum(II) 2,4-pentanedionate and tris(trimethylsilyl)phosphine ($(Me_3Si)_3P$) are employed in a hot-injection synthesis to allow for separate control of the nucleation and growth processes. In a typical preparation, 0.3 mmol of platinum(II) 2,4-pentanedionate (0.118 g) was initially mixed with 8 mL oleylamine (OAm), 0.5 mL oleic acid (OA), and 8 mL octadecene (ODE). Oxygen and impurities were removed by placing the solution under vacuum at 120 °C for 1 h. In a nitrogen atmosphere, the solution was then heated to 220 °C at a rate of 10 °C/min. Meanwhile, the P precursor was prepared by placing 1.2 mL $(Me_3Si)_3P$ dissolved in hexane (10 wt%) and 1.0 mL ODE under vacuum to remove the hexane at room temperature. The $(Me_3Si)_3P$ solution was quickly injected at 220 °C and for 15 min the temperature was maintained. Inductively coupled plasma mass spectroscopy (ICP–MS) gives an atomic ratio of platinum to phosphorus of 0.498 (Supplementary Table 1), and energy-dispersive X-ray spectroscopy (EDS) of platinum phosphide NCs shows a similar Pt:P ratio of

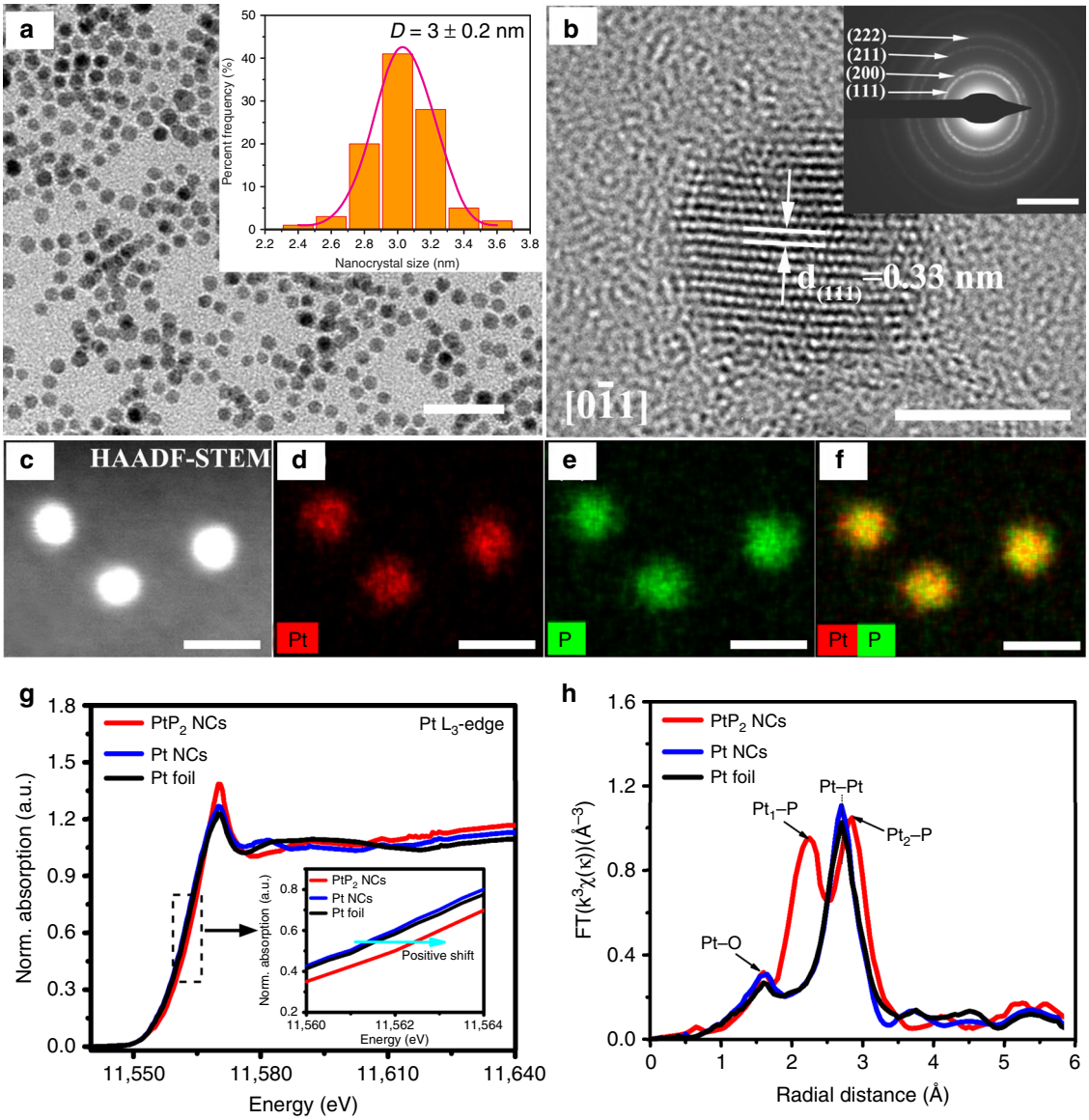

Fig. 1 Materials characterization of PtP_2 NCs. a TEM image; scale bar, 20 nm. **b** HRTEM image; scale bar, 2 nm, inset is the selected-area electron diffraction (SAED) image; scale bar, 5 1/nm. **c** HAADF-STEM, and **d**–**f** elemental mapping images of PtP_2 NCs; scale bar, 5 nm. **g** Pt L_3-edge X-ray absorption near-edge structure (XANES) and **h** extended X-ray absorption fine structure (EXAFS) spectra of PtP_2 NCs, Pt NCs, and Pt foil.

0.509 (Supplementary Fig. 1), confirming the formation of PtP_2. The XRD pattern of PtP_2 NCs matches the cubic structure of bulk PtP_2 (ICDD PDF: 01-080-2220) (Supplementary Fig. 2). The central Pt atoms are surrounded by 6 phosphorus atoms, which are situated at the corners of a slightly distorted octahedron. Similarly, the phosphorus atoms are surrounded by one phosphorus and three platinum neighbors (Supplementary Fig. 3). The transmission electron microscopy (TEM) image of the as-synthesized PtP_2 NCs shows a spherical morphology with average size of 3 ± 0.2 nm (Fig. 1a). A well-resolved lattice fringe with interplane distances of 0.33 nm is observed, corresponding to the (111) crystallographic plane of the cubic PtP_2 (Fig. 1b). The (111) plane, associated with other planes, such as (200), (211), and (222), are shown on the corresponding selected-area electron diffraction (SAED) image (inset of Fig. 1b), indicating good crystallinity of the as-synthesized PtP_2 NCs. The well-defined spherical geometry and high monodispersity of the PtP_2 NCs is clearly observed from the high-angle annular dark-field scanning TEM (HAADF-STEM) image (Fig. 1c). The elemental mapping of the PtP_2 NCs shows that the Pt and P elements are evenly distributed throughout the whole nanocrystal region (Fig. 1d–f).

X-ray absorption spectroscopy was carried out to reveal the local geometric and electronic structures of PtP_2 and Pt NCs. Figure 1g shows the Pt L_3-edge X-ray absorption near-edge structure (XANES) spectra of PtP_2 NCs, Pt NCs, and Pt foil. The rising edge of PtP_2 NCs shows a positive shift compared with that of Pt NCs and Pt foil due to the increased valence oxidation state after incorporation of P into Pt. This result can be ascribed to an electron density shift from metallic Pt to local P atoms with high electronegativity. The donor-acceptor nature of electron density distribution in PtP_2 NCs is further confirmed by the X-ray photoelectron spectroscopy (XPS) of Pt 4f (Supplementary Fig. 5). The binding energy of Pt $4f_{7/2}$ for PtP_2 NCs is positively shifted (0.9 eV) from that of Pt $4f_{7/2}$ for Pt NCs. This shift is larger than that of conventional metal alloying, suggesting that the stronger electron delocalization in PtP_2 NCs may have greater influence on the intrinsic electronic properties and reaction intermediates

adsorption/desorption behavior[28]. The intensity of the Pt L_3 white line is a qualitative indicator of electron vacancies in the 5d orbitals of Pt atoms. The white line intensity for PtP_2 NCs is higher than that for Pt NCs and Pt foil, which is attributed to an electron density shift from Pt to P which creates electron vacancies in Pt and increases probability for electron transition from 2p to the unoccupied 5d orbital[29]. The Fourier transforms of the k^3-weighted extended Pt L_3-edge X-ray absorption fine structure (EXAFS) spectra were shown in Fig. 1h. The EXAFS fitting results are summarized in Supplementary Fig. 6 and Table 2. The small peak located at 1.60 Å is assigned to the typical Pt–O bond which is derived from trace amounts of surface platinum oxide. The peaks at 2.25 and 2.85 Å are both attributed to the Pt–P bond, suggests diverse P coordination to the central Pt. Interestingly, no fitting peak is observed within 3.00 Å for the Pt-Pt bond in PtP_2, which is consistent with an expected Pt-Pt distance in the range of 3.6–4.2 Å in the PtP_2 cubic crystal structure. This length difference has significant influence on the intermediate adsorption on the platinum bridge site, which will be discussed in detail later.

Electrochemical ORR performance. The ORR was performed in O_2-saturated 0.1 M $HClO_4$ solution using a RRDE. The potential of the ring is set such that it can oxidize the H_2O_2 produced at the disk electrode, with the resulting current providing a measurement of the level of H_2O_2. For the disk current, the PtP_2 NCs show an onset potential (defined as the potential at which a current density of 0.1 mA/cm^2 is achieved) of 0.716 V vs. RHE, which is significantly shifted from that of Pt NCs (0.88 V vs. RHE) (Fig. 2a). A remarkable ring current in the potential range of 0.1–0.708 V vs. RHE is observed on PtP_2 NCs, compared to a negligible current measured for the Pt NCs control. The slightly higher onset potential of the PtP_2 NCs than the thermodynamic limit of 0.70 V vs. RHE could potentially be ascribed to a Nernst-related potential shift. The PtP_2 NCs achieve a maximum H_2O_2 selectivity of 98.5% at 0.27 V vs. RHE, and the corresponding electron transfer number (n) is 2.03 (Supplementary Fig. 8), while the Pt NCs follow a typical four-electron pathway during ORR process. This indicates that phosphorus incorporation can regulate the electronic structure of surface Pt active sites and therefore alter the ORR pathway. Figure 2b summarizes the mass activity of different electrocatalysts for O_2-to-H_2O_2 conversion, and further details of these calculations are available in Supplementary Table 3. The remarkable mass activity and low overpotential of PtP_2 is superior to most reported electrocatalysts. While it is inferior to the state-of-the-art Pt–Hg and Pd–Hg alloys, replacement of Hg with minimal loss in efficiency is promising since the potential for Hg to leach directly into a medicinal product is a considerable barrier for practical application.

To directly compare stability, highly monodispersed Pt–Hg nanocrystals were also synthesized (Supplementary Fig. 9). The PtP_2 NCs show very similar mass activity to the-state-of-art Pt-Hg NCs (Supplementary Fig. 10), but the leaching of heavy metals is greatly reduced as determined by ICP–MS. The concentration of Hg leached from Pt–Hg NCs is 74.6×10^3 ppb after ORR for 6 h in 0.1 M $HClO_4$, which is three orders of magnitude higher than the Pt and P leached from PtP_2 NCs (Supplementary Table 4). This severe leaching phenomenon limits the wide application of H_2O_2 produced by the Pt–Hg nanoparticle electrocatalyst, particularly for medicine or water purification. In general, the chemical stability of bimetallic Pt–Hg alloy catalysts is highly dependent on their synthesis routes and surface properties and further studies need to be done to systematically establish Hg leaching discrepancy between the discussed Pt–Hg NCs and the reported electrodeposited Pt–Hg nanoparticles[6].

In situ attenuated total reflection infrared spectroscopy (ATR-IR) was carried out to investigate adsorbed oxygen intermediates on the supported PtP_2 catalyst during ORR in O_2-saturated 0.1 M $HClO_4$ (Fig. 2c). As detailed below, the in situ observation of OOH_{ad} and $HOOH_{ad}$ during ORR confirms the associative two-electron pathway for PtP_2. In accordance with previous literature, the bands at 1435 and 1330 cm^{-1} are assigned to the functional groups of the carbon support, and the bands at 1126 and 1052 cm^{-1} are ascribed to the ClO_4^- species[30]. The absorption band at 1488 cm^{-1}, present at all applied potentials, is assigned to the O–O stretching mode of adsorbed molecular oxygen ($O_{2,ad}$). This assignment agrees with previous report that the band of adsorbed O_2 is observed around 1468 cm^{-1} for Pt/C[31]. The band intensity shows a continuous decrease with increase of overpotential due to O_2 consumption as well as substitution by the newly formed oxygen species (Supplementary Fig. 11a). This band disappears in N_2-saturated solution and shifts to 1406 cm^{-1} in the $^{18}O_2$ isotope spectrum (Supplementary Fig. 12). The band at 1264 cm^{-1} can be assigned to the O–O stretching mode of adsorbed superoxide (OOH_{ad}), which is consistent with that reported for the Au electrode[32]. It appears at 0.7 V vs. RHE and increases with increasingly negative potential (Supplementary Fig. 11b), which is consistent with the trend of the H_2O_2 current in the linear sweep voltammograms of PtP_2 NCs. The OOH_{ad} band shows a significant shift to 1193 cm^{-1} in $^{18}O_2$ (Supplementary Fig. 10), while remaining the same in the deuterated medium (Supplementary Fig. 13). As for Pt NCs, the OOH_{ad} band is initially observed at 0.9 V vs. RHE, consistent with its onset potential of four-electron ORR. Lastly, the band at 1396 cm^{-1} is attributed to the OOH bending mode of adsorbed hydroperoxide ($HOOH_{ad}$)[33]. A slight shift is observed for $HOOH_{ad}$ in $^{18}O_2$ (Supplementary Fig. 12), while the band is not detected in the deuterated medium presumably due to a large shift to lower wavenumber (Supplementary Fig. 13). The $HOOH_{ad}$ band first appears at 0.7 V vs. RHE for PtP_2 NCs, in accordance with the onset in H_2O_2 production.

Figure 2d shows the normalized in situ Pt L_3-XANES spectra of PtP_2 NCs recorded at various ORR potentials in 0.1 M $HClO_4$. Commercial PtO_2, $PtCl_2$, and Pt foil were used as references and a linear combination of XANES spectra was fitted to the in situ Pt L_3-edge spectra (Supplementary Figs. 14 and 15). The calculated oxidation states of platinum species in PtP_2 under various potentials are shown in Fig. 2e and summarized in Supplementary Table 5. For the as-prepared PtP_2 NCs, the initial oxidation state of platinum species is calculated to be +3.26, which is attributed to the electron density shift from Pt to P. Under open-circuit potential (OCP) and 0.9 V, a slight change of oxidation state is observed. This is presumably attributed to the formation and dissolution of minor surface oxide based on the small change of white line intensity. At a potential of 0.7 V a negative shift in the absorption edge is observed the average oxidation state decreases to +2.72 since the surface platinum active sites in PtP_2 start to be involved in O_2 activation and H_2O_2 generation. The oxidation state further decreases to +2.25 by 0.5 V and remains the same to 0.3 V. It should be noted that the oxidation state of +2.25 keeps stable at 0.3 V for 6 h of measurement (Supplementary Fig. 16), indicating that the high P content can stabilize $Pt^{+2.25}$ in the PtP_2 for sustaining rapid and stable O_2-to-H_2O_2 conversion.

The inset of Fig. 2d illustrates the changes in the Pt L_3-edge XANES spectra with the in situ potential. Here, $\Delta\mu$ is the value obtained by subtracting the Pt L_3-edge XANES spectrum at 0.54 V from that collected at elevated potentials. The $|\Delta\mu|$ of Pt NCs increase monotonically with potential, while for PtP_2 $|\Delta\mu|$

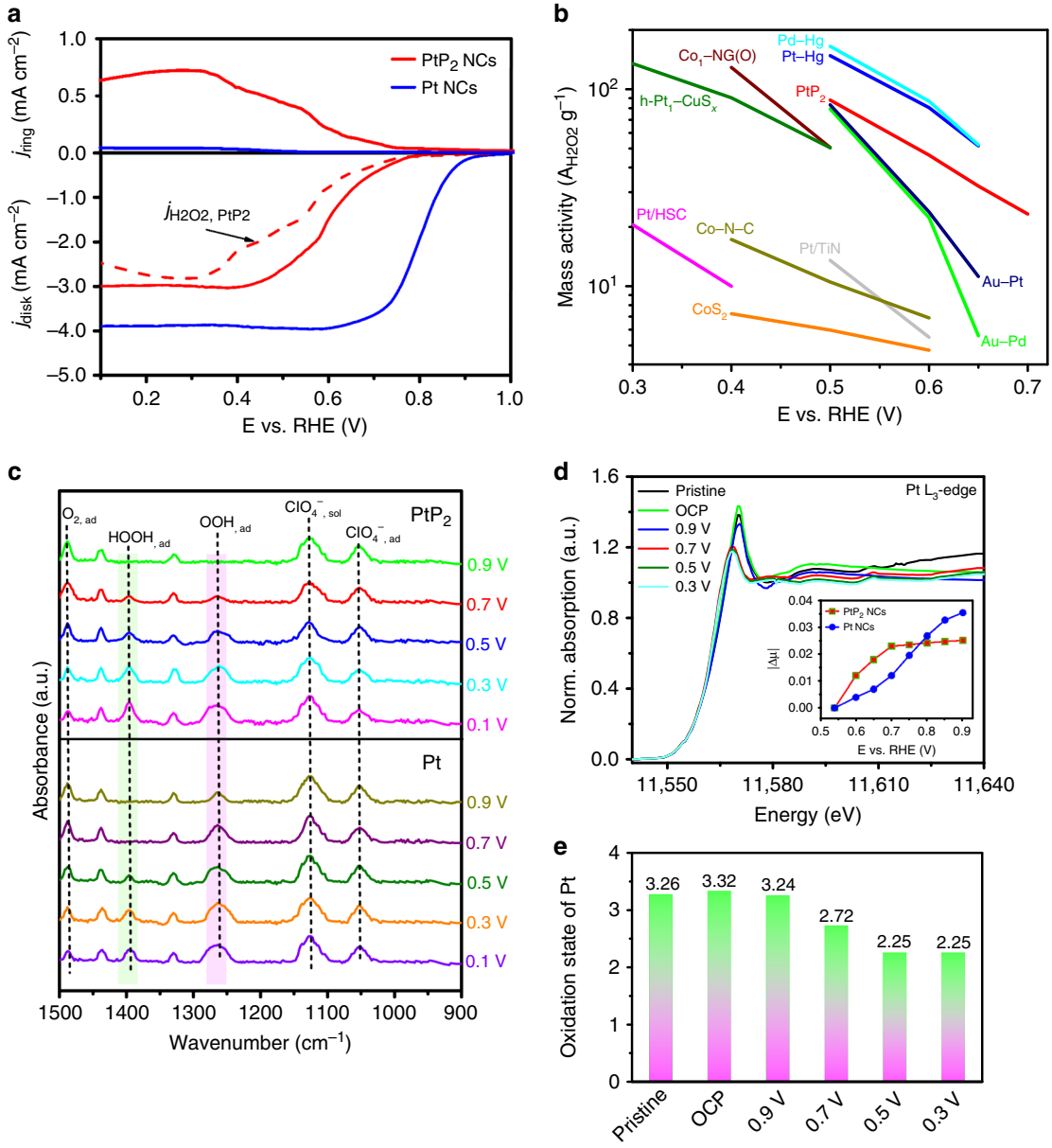

Fig. 2 Electrochemical and in situ characterization of PtP_2 NCs. a RRDE voltammograms at 1600 rpm in O_2-saturated electrolyte with the disk current density, ring current density, and current density corresponding to hydrogen peroxide obtained from the ring current. **b** Mass activity of different electrocatalysts for H_2O_2 production in acidic electrolyte. **c** In situ ATR-IR spectra and **d** in situ Pt L_3-edge XANES spectra collected on the PtP_2 electrodes at constant potential in O_2-saturated 0.1 M $HClO_4$. Inset in **d** shows the impact of potential on the Pt L_3-edge XANES spectra: $\Delta\mu = \mu(V) - \mu(0.54\,V)$. **e** Pt oxidation state in PtP_2 as a functional of applied constant potential.

increases sharply from 0.54–0.7 V but remains unchanged to 0.9 V. The value of $|\Delta\mu|$ is expected to increase with increasing amounts of oxygen species adsorption[34]. The relatively high $|\Delta\mu|$ for PtP_2 within 0.54–0.7 V indicates a high coverage of oxygen intermediates in this region of intermediate activity, potentially due a rate limiting step beyond generation of the initial oxygen intermediates such as *OOH adsorption.

Theoretical DFT calculation for ORR. Two-electron ORR generally follows two hydrogenation steps for H_2O_2 production, i.e., $O_2 \rightarrow OOH^* \rightarrow H_2O_2$, while four-electron ORR proceeds with four successive hydrogenation steps for H_2O generation, i.e., $O_2 \rightarrow OOH^* \rightarrow O^* \rightarrow OH^* \rightarrow H_2O$ (Fig. 3a). The optimized geometries of OOH*, O*, and OH* intermediates on PtP_2 (111) are shown in Supplementary Fig. 17. Recent theoretical studies have pointed out that the ORR activity for H_2O_2 production is strongly related to the binding ability of OOH*[6]. Specifically, for an ideal catalyst for H_2O_2 production, the adsorption of OOH* should be neither too strong nor too weak.

The adsorption configuration of OOH* is determined by the orientation type of the adsorbed oxygen molecule. There are usually two different adsorption configurations, end-on adsorption and side-on adsorption, for O_2 on the catalytic surface of Pt and PtP_2 (Supplementary Fig. 18). For pure Pt, the optimized adsorption energy (E_{ads}) of the end-on configuration is more negative than that of side-on configuration, indicating that the former orientation is more favorable and subsequently that associative hydrogenation prevails over the dissociative reaction pathway. For PtP_2, the adsorption energy of the end-on

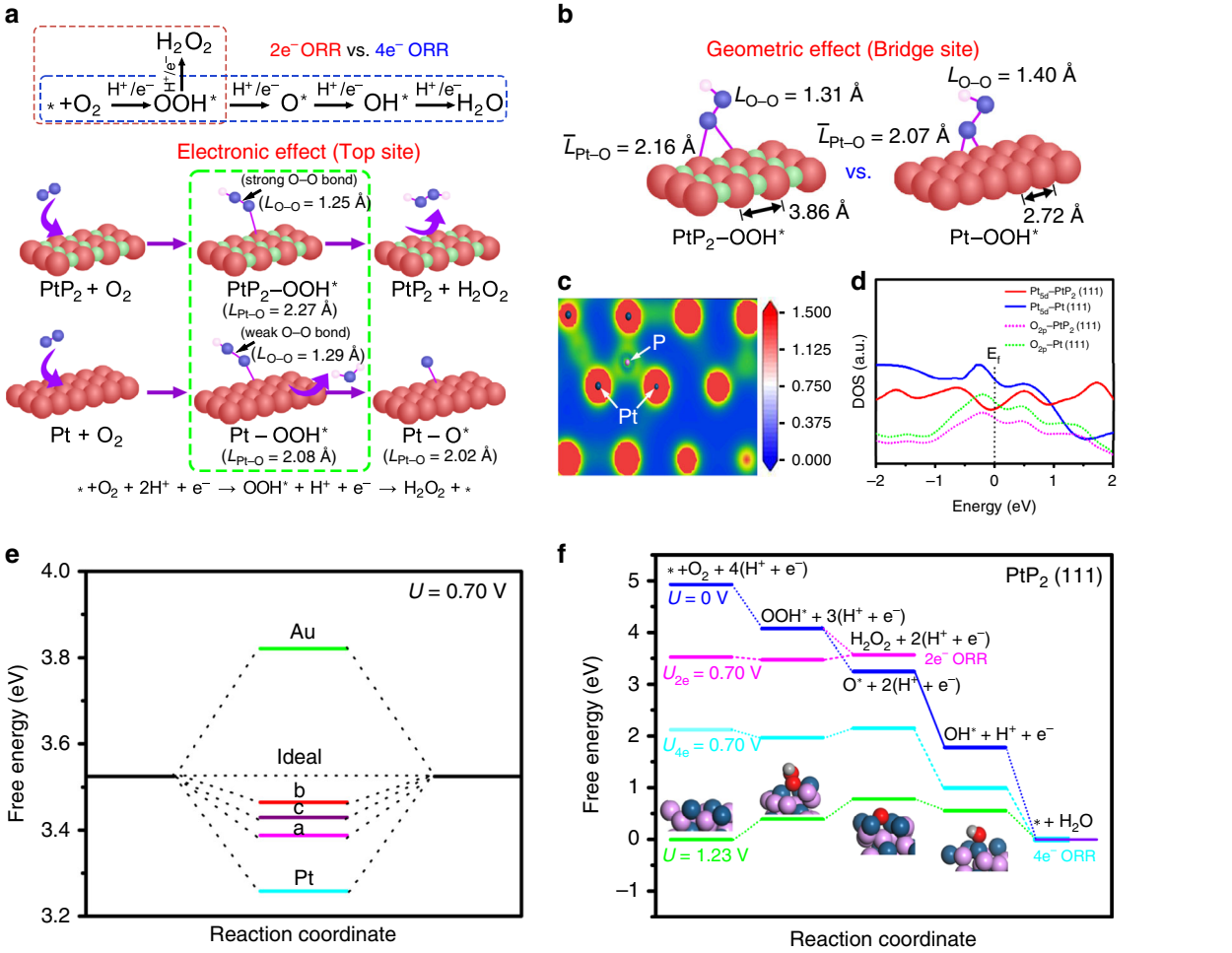

Fig. 3 DFT analysis of reaction intermediates. a Key oxygen intermediates for PtP_2 and Pt during two-electron and four-electron ORR pathways. OOH* adsorbed on top site of PtP_2 and Pt is compared. **b** Difference between adsorption behavior of OOH* on bridge site of PtP_2 and Pt. **c** Bader charge distribution of PtP_2. **d** Partial density of states (PDOS) for PtP_2 (111) and Pt (111) with adsorbed OOH*. **e** Free-energy diagram for O_2-to-H_2O_2 at 0.70 V. **f** Free-energy diagram for the two-electron and four-electron ORR on PtP_2.

configuration is three times that of side-on configuration, suggests that the side-on adsorption of O_2 is less favored to occur on the PtP_2 surface and therefore the end-on adsorption of OOH* become the dominating configuration. Moreover, the optimized adsorption configuration of O* on PtP_2 (111) is only available on top and bridge sites since simulations of O* adsorbed on hollow sites yielded bridge sites following optimization (Supplementary Fig. 17). By contrast, the O* adsorbed on hollow site on Pt (111) is more stable than that on the top and bridge sites because of strong back electron donation from Pt to O orbitals in the triple bonding state. However, the O_2 molecule and OOH* intermediate adsorbed on hollow site of Pt (111) surface are less favorable, which leads to higher energy barrier for the conversion of OOH* to O* at the hollow site. Figure 3e depicts the free-energy diagram for two-electron O_2-to-H_2O_2 pathway at equilibrium potential of 0.7 V vs. RHE. The OOH* on the typical Au and Pt metal catalysts is too weak and too strong, respectively. The free energy of OOH* (G_{OOH*}) on top (a), bridge (b), and hollow (c) sites of PtP_2 (111) is 3.39, 3.47, and 3.43 eV, respectively. Compared to Pt, the average free-energy difference compared to the ideal value of 3.52 eV is 0.09 eV, which is less than half that for Pt (0.261 eV). The weaker adsorption of OOH* on PtP_2 (111) can be explained by both electronic and geometric effects resulting from incorporation of P. For the top site of PtP_2 (111), the bond length of Pt–O in PtP_2–OOH* is 2.27 Å, longer than that in Pt–OOH* (2.08 Å) (Fig. 3a). This effect is attributed to electron delocalization in phosphorus-rich PtP_2 (Fig. 3c). For the bridge site of PtP_2 (111), the average Pt–O bond length is increased because the Pt–Pt distance is larger due to the high degree of P incorporation (Fig. 3b).

A lower overlap among the binding states between Pt_{5d} and O_{2p} is observed when OOH* is adsorbed on PtP_2 (111) compared with Pt (111) (Fig. 3d), leading to a weaker binding strength of OOH* over PtP_2 (111) surface. Figure 3f shows the potential-dependent free-energy diagram for two-electron and four-electron ORR pathways on the PtP_2 (111) surface. At zero electrode potential ($U = 0$ V) all elementary steps of the ORR are exothermic. At the equilibrium potential ($U = 1.23$ V), based on the free energies of the intermediates species the first two steps are predicted to be rate determining for the four-electron ORR. At an electrode potential of 0.7 V, the free-energy difference between OOH* to H_2O_2 is 0.106 eV compared to 0.180 eV for that of OOH* to O*, consistent with the experimental observation that the adsorbed OOH* preferentially undergoes hydrogenation to form H_2O_2 rather than continuing the dissociation path under a small overpotential. This result can be understood not only by the weakening of the Pt–OOH* bond, but also by the tightening of the O–O bond in OOH* adsorbed to PtP_2 relative to *OOH adsorbed on Pt. For both the top and bridge sites on PtP_2, the O–O bond length of adsorbed OOH* is

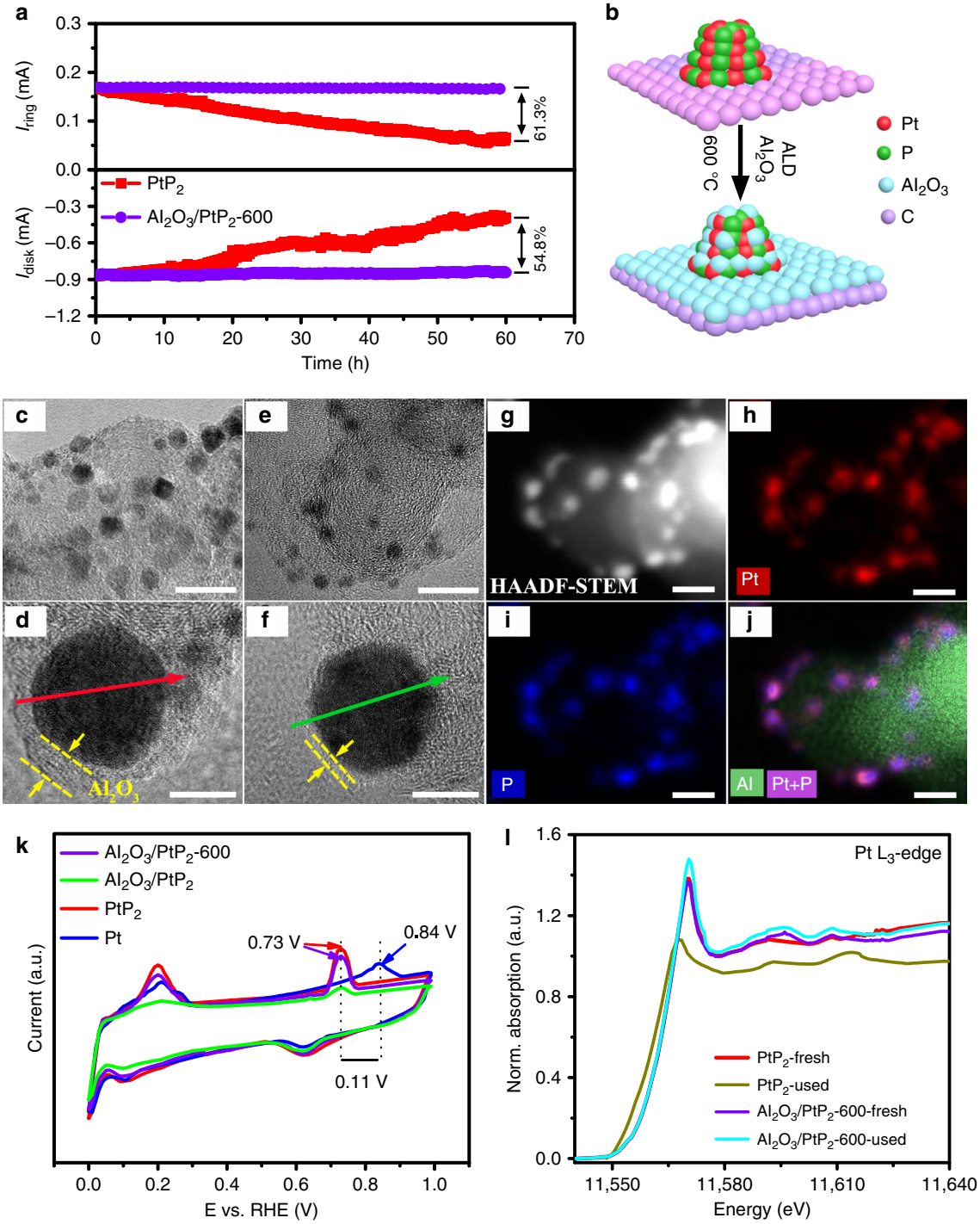

Fig. 4 Stabilization of NCs by ALD of Al_2O_3. **a** Disk and ring current stability of PtP_2 and Al_2O_3/PtP_2-600 measured at a constant potential of 0.4 V vs. RHE for 60 h. **b** Depiction of Al_2O_3 coating by ALD and subsequent activation. TEM images for **c**, **d** Al_2O_3/PtP_2 and **e**, **f** Al_2O_3/PtP_2-600; scale bar, **c**, **e** 20 nm; **d**, **f** 3 nm. **g**–**j** HAADF-STEM image and corresponding elemental mapping for Al_2O_3/PtP_2-600; scale bar, 10 nm. **k** Electrochemical CO stripping tests and **l** Pt L_3-edge XANES spectra of as-prepared samples before and after ORR.

shorter than that on Pt, which is beneficial to suppress the OOH*-to-O* dissociation tendency.

ALD overcoat for stabilization of ultrasmall PtP_2 NCs. Although the ultrasmall PtP_2 NCs gave efficient and selective O_2-to-H_2O_2 conversion, both the disk and ring current quickly decayed and around 60% activity was lost within 60 h at an applied potential of 0.4 V vs. RHE (Fig. 4a). Considering that the elemental composition, crystalline structure, and surface electronic structure of PtP_2 all remain the same following the stability test (Supplementary Fig. 19), the degradation is ascribed to size instability, which leads to nanocrystal aggregation (Supplementary Fig. 20) and a significant decrease in the electrochemical active surface area (EASA, Supplementary Fig. 21). The left shift of Pt L_3-rising edge of XANES is also attributed to small size nanocrystal aggregation (Fig. 4l). Ultrathin metal oxides by ALD

have been applied to encapsulate the supported nanoparticles and improve the size stability of nanoparticle catalysts[35,36]. In order to minimize additional electrocatalytic effects from ALD overcoating layer, we chose the relatively inert Al_2O_3 rather than the typical transition metal oxide promotors (e.g., Co_3O_4[37], MnO[38], Fe_2O_3[39], and MoO_3[40]). ALD of a thin Al_2O_3 layer was carried out to stabilize the ultrasmall PtP_2 NCs on a commercial carbon support by alternately exposing the sample to cycles of trimethylaluminum (TMA) and water at 175 °C (Fig. 4b). Figure 4c shows that the average size of PtP_2 NCs is increased to 5.2 ± 0.4 nm due to minor thermal aggregation during the mild-ALD process. The Al_2O_3 overcoat thickness is 1.8 ± 0.2 nm after 42 cycles (Fig. 4d, Supplementary Fig. 22a). This overcoat thickness is smaller than that expected for the typical ALD growth rate for Al_2O_3 of 1.19 Å $cycle^{-1}$, ascribed to the site blocking from any hydrophobic organic ligands remaining on the PtP_2 NCs surface (Supplementary Fig. 23). We determined that 42 cycles of ALD Al_2O_3 is required to stabilize PtP_2 NCs and maintain ORR durability, but without further processing the ring current shows a 32.5% decrease compared to the uncoated sample (Supplementary Fig. 24). An observed decrease in EASA is consistent with an expected blocking of active sites by the ALD layer (Supplementary Fig. 25). A balance between increasing the stability and maintaining high activity is achieved by annealing the sample following ALD at 600 °C in N_2 gas for 2 h. The size dispersity and element distribution are well maintained (Fig. 4e, g–i), while the overcoat thickness is diminished (~0.54 nm) (Fig. 4f, Supplementary Fig. 22b) and the EASA and Brunauer–Emmett–Teller (BET) surface area is almost restored (Supplementary Fig. 25). The disk and ring current of the annealed sample (Al_2O_3/PtP_2–600) remain the same before and after 60 h of ORR testing in 0.1 M $HClO_4$ (Fig. 4a), indicating that the Al_2O_3 overcoat and activation can stabilize the PtP_2 NCs, while maintaining open pathways to the NC surface (Supplementary Fig. 26). It should be noted that the O_2-to-H_2O_2 selectivity is nearly the same after the ALD surface modification, indicating that the ultrathin Al_2O_3 overcoating has a negligible geometric effect on the electrocatalytic selectivity of PtP_2 electrode (Supplementary Fig. 27). The Pt L_3-edge XANES and corresponding EXAFS of PtP_2, Al_2O_3/PtP_2, and Al_2O_3/PtP_2-600 were compared in Supplementary Fig. 28. No change in the absorption edge (E_0) and Pt–P bond distance was observed, which suggests that the intrinsic electronic structures of PtP_2 were well maintained after ALD coating and annealing treatment. This could be further supported by the Pt 4f XPS results (Supplementary Fig. 29). The slight increase for the white line intensity of XANES attributes to the formation of small amount of platinum oxide during ALD process. To further evaluate the effect of the activated coating on the electrochemical properties, CO desorption (Fig. 4k) was studied by electrochemical CO stripping. Prior to the activation step, the shift in the oxidation peak is lost after Al_2O_3 overcoating and the current decreases suggesting the active surface is blocked. We also note that incorporation of P into Pt facilitates CO desorption, as proven by the negative shift of CO oxidation peak (0.11 V) in the CO stripping test (Fig. 4k).

Scalable neutral H_2O_2 electrosynthesis. Having developed a stable and selective electrocatalyst for O_2-to-H_2O_2 conversion, we further incorporated our catalyst into a practical polymer electrolyte membrane fuel cell (PEMFC) to synthesize a neutral H_2O_2 solution at high concentration and volume. Figure 5a shows a schematic diagram of a PEMFC using commercial Pt/C anode for H_2 oxidation, Nafion 117 membrane for proton transportation and elimination of gas crossover, and our Al_2O_3/PtP_2-600 cathode for two-electron ORR. The details of the expeirmental setup and operation are shown in Supplementary Fig. 31. The Al_2O_3/PtP_2-600 catalyst ink was spray coated onto the carbon gas-diffuse layer (GDL) and hot pressed with the Nafion membrane to form the MEA. The overall MEA is compactly connected and no voids are observed between the interfaces (Fig. 5b, c). The Pt, P, and Al elements are well distributed across the MEA (Fig. 5d–f). The optimized conditions (e.g., mass loading, catalyst support, water flow rate, and operation temperature) for H_2O_2 production in PEMFC are summarized in Supplementary Table 6. The optimized mass loading of Al_2O_3/PtP_2-600 is determined to be 0.8 mg cm^{-2} (Supplementary Fig. 32), as lower loading leads to kinetics loss and higher loading causes high O_2 gas mass transport reisistance[41]. The current efficiency (CE%) and H_2O_2 production rate ($r(H_2O_2)$) at 50 mA cm^{-2} is 60.8% and 0.57 mmol h^{-1} cm^{-2}, respectively. A high CE is achieved despite the more challenging kinetics for H_2O_2 production at neutral conditions compared to the commonly used acidic conditions. At high current density, cathode flooding is typically observed in carbon-based GDE due to the loss of hydrophobicity during PEMFC operation[42]. For the PEMFC with 20 wt% teflon-treated GDL, the operating current density can be increased up to 125 mA cm^{-2} with significantly improved r (H_2O_2) (1.51 mmol h^{-1} cm^{-2}) compared to that with the non-teflon-treated GDE (Supplementary Fig. 33). Both the highest CE% and $r(H_2O_2)$ are achieved at a water flow rate of 10 mL min^{-1} (Supplementary Fig. 34). Increasing the water flow rate within 2–10 mL min^{-1} is beneficial to remove the generated H_2O_2 and minimize its thermochemical decomposition and/or further electroreduction[27]. However, further increasing the water flow rate to 20 mL min^{-1} reduces the CE% and $r(H_2O_2)$, which is ascribed to the O_2 mass transport being poor under high volume water flow. The optimized temperature is only 40 °C. Increasing operating temperature would improve proton conductivity in the MEA, but the dominant effect is to increase H_2O_2 thermochemical decomposition[25]. Overall, the optimized operation conditions of PEMFC for O_2-to-H_2O_2 are catalyst loading of 0.8 mg cm^{-2}, 20 wt% teflon-treated carbon GDL, water carrier flow rate of 10 mL min^{-1}, and operation temperature of 40 °C. A maximum $r(H_2O_2)$ of 2.26 mmol h^{-1} cm^{-2} is obtained with the PEMFC operating at 150 mA cm^{-2} with a highest CE of 78.8% (Fig. 5g). The difference in CE for of O_2-to-H_2O_2 in RRDE and MEA system is attributed by the transport efficiency of H_2O_2 away from the electrode surface[2]. In the RRDE, the small amount of generated H_2O_2 molecules are rapidly transported away from the disk electrode and oxidized at the ring electrode, leading to a low steady-state surface H_2O_2 concentration. By contrast, the H_2O_2 molecules produced at the catalyst/membrane interface in the MEA system need a longer time to diffuse though the catalyst layer and gas diffusion layer before removal into the water stream, which causes a higher local concentration of H_2O_2 at the vicinity of catalyst surface and increases the possibility of further H_2O_2 reduction[27]. Moreover, nearly no degradation of the H_2O_2 concentration (14.7 mmol L^{-1}, pH = 6.8) is observed at a constant potential of 0.4 V in 120 h (Fig. 5h). The compact interfaces for both cathode/electrolyte and anode/electrolyte are well maintained after 120 h of measurement (Supplementary Fig. 35). For comparison, a Pt–Hg NC-based MEA was fabricated in the same way and run in the PEMFC under the same conditions. The concentration of leached Hg is 5.9×10^3 ppb in neutral H_2O_2 catholyte solution (Supplementary Table 7), and approximately 38% degradation for H_2O_2 concentration was observed after 6 h of PEMFC operation without recycling of the product (Supplementary Fig. 36). To obtain a neutral H_2O_2 solution with high concentration, the product was recycled to run through the catalyst multiple times, following an initial 1 h run to accumulate 600 mL H_2O_2 solution. Under recycling the accumulated H_2O_2 concentration is increased with the operation time and approaches to 1.21 mol L^{-1} for 120 h. It should be noted that a

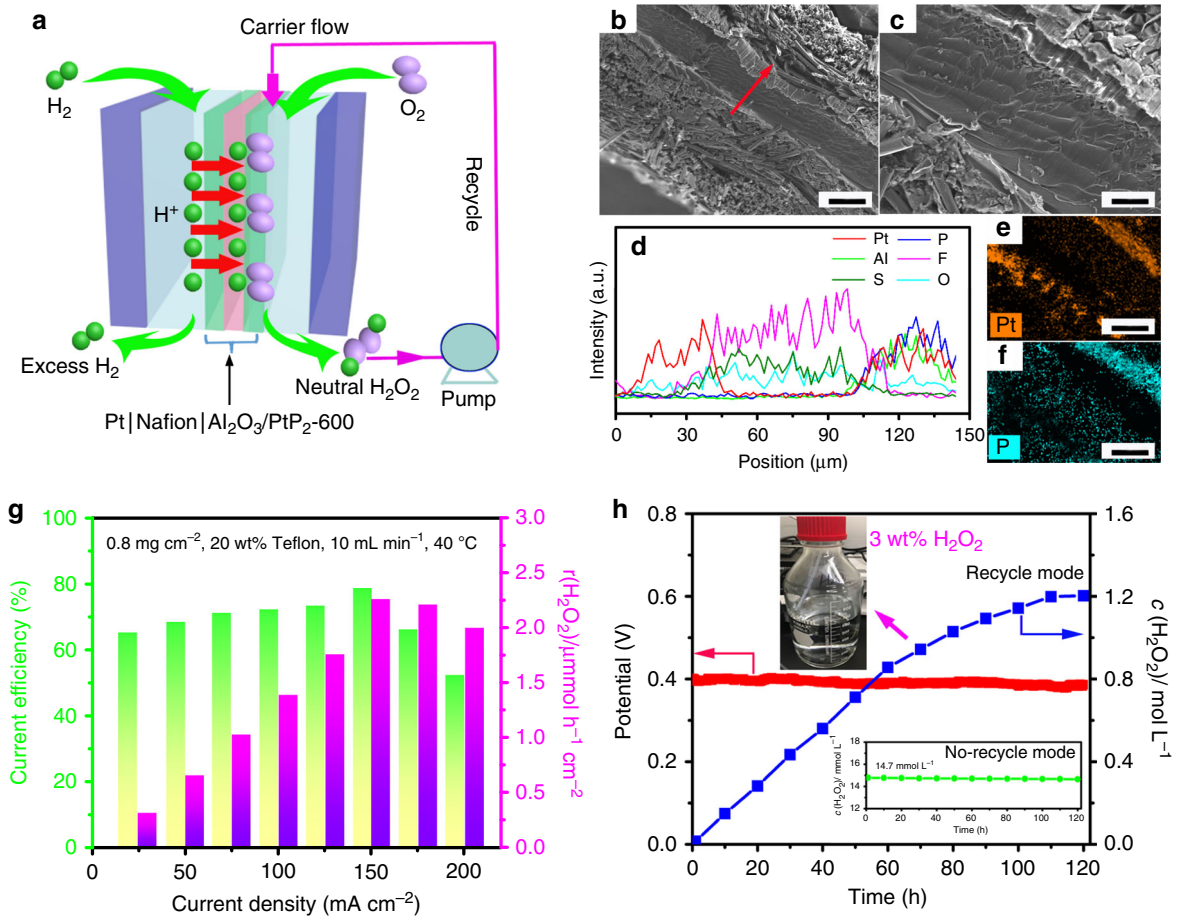

Fig. 5 Performance of polymer electrolyte membrane fuel cell (PEMFC). a Schematic diagram of PEMFC for O_2-to-H_2O_2 production with product recycling. **b**, **c** Cross-sectional SEM images; scale bar, **b** 100 μm; **c** 20 μm. **d** line-scan elemental distribution, and **e**, **f** elemental mapping of Al_2O_3/PtP_2-600 based MEA; scale bar, 50 μm. **g** Current efficiency and H_2O_2 production rate as a function of current density under optimized conditions. **h** Time-dependent neutral H_2O_2 concentration measured at a constant potential of 0.4 for 120 h. The accumulated H_2O_2 concentration in 600 mL when the product is continuously cycled through the system. Concentration reaches a metric value of 3.0 wt% after 65 h (inset of Fig. 5h).

H_2O_2 concentration of 3.0 wt% (pH = 6.6) in 600 mL is achieved after 65 h, sufficient for medical sterilization, chemical synthesis, and food processing. The saturation in the accumulated H_2O_2 concentration is attributed to competing thermochemical and/or electrochemical degradation pathways of H_2O_2. To elucidate the degradation pathways, the electrolysis under recycled operation was conducted in an O_2-free 1 M H_2O_2 solution at the same conditions in PEMFC. The time-dependent H_2O_2 concentration is shown in Supplementary Fig. 37. At open-circuit voltage, the decrease of H_2O_2 concentration is mainly caused by thermochemical reduction and only 48% H_2O_2 remains after 60 h recycling. At 0.4 V vs. RHE, both the thermochemical and electrochemical reduction processes contribute to H_2O_2 degradation. Notably, the electrochemical reduction rate of H_2O_2-to-H_2O is much slower than that of thermochemical reduction, which significantly reduces the consumption of produced H_2O_2 and leads to high saturation levels of H_2O_2 accumulation during electrolyte recycling. A similar recycling strategy for making high concentration H_2O_2 solution from O_2 electroreduction in PEMFC was also demonstrated in previous work[27].

In summary, monodisperse colloidal platinum diphosphide (PtP_2) NCs applied as efficient two-electron ORR electrocatalysts. The PtP_2 NCs require a near-zero overpotential for H_2O_2 initialization and achieve a maximum O_2-to-H_2O_2 selectivity of 98.5% at 0.27 V vs. RHE. DFT results suggest that weakened binding of the OOH* intermediate and inhibition of subsequent O–O breakage of OOH* compared to pure Pt. A PEMFC with Al_2O_3/PtP_2-600 as the cathode catalyst achieves a maximum r (H_2O_2) of 2.26 mmol h^{-1} cm^{-2}, a CE up to 78.8%, and sufficient stability to achieve an accumulated neutral H_2O_2 concentration of 1.21 mol L^{-1} by 120 h. This work provides insight into the development of efficient and stable electrocatalysts for selective production of neutral H_2O_2 in a practical device.

Methods

Chemicals and materials. Oleylamine (OAm, tech. 70%), oleic acid (OA, tech. 90%), 1-octadecene (ODE, tech. 90%), Nafion 117 solution, Teflon dispersion, and commercial Pt/C (20 wt%) were purchased from Sigma-Aldrich. Platinum(II) 2,4-pentanedionate was from Alfa Aesar. Tris(trimethylsilyl)phosphine ($(Me_3Si)_3P$) was purchased from Strem Chemicals. Commercial carbon black, GDL, and Nafion 117 membrane were obtained from FuelCellStore.

Synthesis of platinum diphosphide (PtP_2) NCs. A solution of platinum(II) 2,4-pentanedionate (0.3 mmol), OAm (8 mL), OA (0.5 mL), and ODE (8 mL) was placed into a round bottom flask with a stir bar and degassed at 120 °C under vacuum for 1 h. To prepare for injection of the P source, the solution was then heated to 220 °C under nitrogen. Meanwhile, the P precursor was prepared by placing 1.2 mL $(Me_3Si)_3P$ dissolved in hexane (10 wt%) and 1.0 mL ODE under vacuum to remove the hexane at room temperature. The $(Me_3Si)_3P$ solution was quickly injected at 220 °C and for 15 min the temperature was maintained. To facilitate Ostwald ripening, during cooling the system was kept at 120 °C for 10 min prior to cooling to room temperature. To purify, the precipitate was collected following centrifugation at 6000 rpm for 6 min and redispersed with hexane. To further purify the NCs, aggregation was induced with a 1:6:1 (v:v:v) hexanes:acetone:methanol solution followed by centrifuged and resuspension

with hexane and this procedure was then repeated for a total of four times. The final suspension yield a solution with NC density by weight of 2 mg/mL. For comparison, Pt NCs were synthesized in a similar co-heating way without $(Me_3Si)_3P$ injection. For the synthesis of colloidal Pt–Hg NCs, platinum(II) 2,4-pentanedionate (0.2 mmol), and mercury (II) chloride (0.2 mmol), OAm (4 mL), and ODE (4 mL) were added into a 25 mL reaction flask. The solution was degassed at 120 °C for 1 h and then heated to 200 °C where it was held for 2 h. To facilitate Ostwald ripening, during cooling the system was kept at 100 °C for 10 min prior to cooling to room temperature.

Materials characterizations. Elemental analysis was performed using ICP–MS (Teledyne Leeman Labs). A Bruker D2 Phaser was used to collecte X-ray diffraction (XRD) using Cu Kα radiation. High-resolution transmission electron microscopy (HRTEM) was performed with a Tecnai G2 F20 microscope at 200 or 300 kV. STEM was done using a JEOL JEM 2200FS STEM/TEM microscope at an acceleration voltage of 200 kV equipped with a CEOS probe corrector (Heidelberg, Germany). For EDS a Bruker-AXS silicon drift detector was used. An Autosorb-iQ from Quantachrome was used to find the BET surface area from nitrogen adsorption isotherms. XPS was performed with a Kratos Axis Ultra DLD, UK, and the C 1s peak at 284.8 eV was used for calibration. In situ and ex situ Pt L_3-edge XAFS measurements were made at the beamline 14W1 in Shanghai Synchrotron Radiation Facility (SSRF), China. PtO_2, $PtCl_2$, and Pt foil were used for linear combination fitting to calculate the Pt valence oxidation state. XANES calculations were done using the FEFF8.2 code and the multiple-scattering method. The experimental absorption coefficients are reported as normalized absorption following background subtraction.

Catalyst inks and electrode preparation. The NCs were combined with an equal amount by weight of Ketjen carbon (C) and sonicated for 1 h (5 mL of 2 mg mL^{-1} NC solution with 10 mg of C support). To remove excess ligands, the hexane was allowed to evaporate and the catalyst was maintained at 60 °C for 2 h in acetic acid (8 mL). This solution was then centrifuged for 5 min at 5000 rpm following addition of 8 mL of ethanol. The collected precipitate was underwent an additional two cycles of the acetic acid treatment. The final catalyst ink (2 mg mL^{-1}) was composed of the purified NCs and isopropanol, water, and Nafion 117 solution (v:v:v = 2:4:0.05). A rotating disk electrode (RDE) with a glassy carbon core was polished by a 0.5 and 0.05 μm alumina powder and rinsed with deionized water. Unless specified, 20 μL of catalyst ink was drop deposited on the glassy carbon working electrode (OD = 6 mm, MTI34 series) with a loading of 0.2 mg cm^{-2}.

Electrochemical measurements. For ORR, all tests were done using a conventional three electrode electrochemical cell with a Biopotentiostat Model AFCBP1 (Pine Instrument Company). The cyclic voltammetry (CV) experiments were performed in N_2- or O_2-saturated 0.1 M $HClO_4$ at room temperature with a scan rate of 10 mV/s. RDE and rotating ring-disk electrode (RRDE) tests were conducted in O_2-saturated 0.1 M $HClO_4$ with a scan rate of 10 mV/s. The RRDE voltammograms were performed with a glassy carbon disk electrode and a Pt ring electrode. Pt foil and Ag/AgCl were used as counter electrode and reference electrode, respectively. Flow of O_2 was maintained into the electrolyte during the entire ORR process to ensure the O_2/H_2O equilibrium. The disk electrode was scanned at a rate of 10 mV/s at 1600 rpm, and the Pt ring electrode potential was fixed at 1.5 V vs. RHE. The hydrogen peroxide yield (%H_2O_2) and electron transfer number (n) were calculated by the following equations:

$$\%H_2O_2 = 200\frac{i_r/N}{i_d + i_r/N} = 200\frac{i_r}{Ni_d + i_r}, \quad (1)$$

$$n = 4\frac{i_d}{i_d + i_r/N} = 4\frac{Ni_d}{Ni_d + i_r}, \quad (2)$$

where i_d and i_r are the disk and ring currents, respectively. N is the Pt ring current collection efficiency. The N value in our system was calibrated in 0.1 M $HClO_4$ with a 10 mM $K_3Fe(CN)_6$ electrolyte and is approximately 0.25 (Supplementary Fig. 38). For the CO striping test, the electrodes were initially immersed in the CO-saturated 0.1 M $HClO_4$ by purging with 10 wt% CO in N_2 gas for 30 min and then set to 0.10 V vs. RHE for 15 min to form a CO adsorption layer on the catalyst surface. Then the electrolyte was purged by N_2 gas for 10 min to remove the remaining CO in solution. The CO stripping CVs were obtained in a potential range of 0–1.2 V with a scan rate of 20 mV/s. Electrochemical impedance spectroscopy was performed on a Reference 600 (Gamry Instrument Inc.) with the working electrode biased at OCP, while sweeping the frequency from 10^5 to 0.1 Hz with a 10 mV AC dither. To determine the electrochemical capacitance, CV scans in the non-faradaic potential region were conducted and the capacitive current was obtained at the middle potential value for each scan rate. CV was carried out in a nitrogen-purged 5 mM $K_3Fe(CN)_6$/0.1 M $HClO_4$ solution with platinum foil as the counter electrode. EASA values were calculated using the Randles–Sevcik equation[43]:

$$I_p = \left(2.36\times 10^5\right)n^{3/2}AD^{1/2}Cv^{1/2}, \quad (3)$$

where I_p is peak current (A), $n = 1$, $D = 4.34 \times 10^{-6}$ cm^2 s^{-1}, A is the EASA (cm^2), C is the concentration of potassium ferricyanide (5×10^{-6} mol cm^{-2}), and v is the scan rate (5 mV s^{-1}). Conversion from vs. Ag/AgCl to vs. RHE was done by adding $0.197 + 0.059 \times$ pH.

For in situ ATR-FTIR measurements, a diamond-like carbon was coated onto a Si wafer ($5 \times 8 \times 1$ mm^3) to prepare the internal reflection element (IRE). The coated IRE was ultrasonicated for 2 min with 30% concentrated H_2SO_4 followed by rinsing with DI water before experiments. A 50 μL of 2 mg mL^{-1} catalyst ink (no Nafion binder) was dropcast on the IRE and dried under air at room temperature. A glassy carbon paper was placed on top of the catalyst layer for good electrical contact. Glassy carbon rod connected to the IRE, Pt gauze, and Ag/AgCl in 3 M KCl were used as the working electrode, counter electrode, and reference electrode, respectively. An FTIR spectrometer with a MCT detector was used for the in situ ATR-FTIR measurements. Solutions were saturated either with O_2 for ORR or with Ar as a control. Gamry Reference 600 potentiostat during recording of the IR spectra.

ALD Al_2O_3 overcoat for stabilization. The ALD Al_2O_3 overcoat for supported PtP_2 was grown in a GEMSTAR-6 atomic layer deposition (ALD) system using trimethylaluminum (TMA) and distilled water (H_2O) at 175 °C. The precursors were kept in the chamber for 2.2 s and a 28 s purge was used. To ensure the deposition occurred with typical growth per cycle, a silicon wafer with native oxide was included alongside the sample as a control and the Al_2O_3 thickness on the wafer was determined by the X-ray reflectivity. After 42 cycles, the overcoated PtP_2 was activated at 600 °C for 2 h in tube furnace under N_2 gas flow (Al_2O_3/PtP_2-600). For comparison, the pure Al_2O_3 thin film with around 2 nm thickness on silicon was fabricated by ALD for 20 cycles.

Scalable H_2O_2 production in fuel cell. The MEA for testing the activity in a H_2–O_2 fuel cell was prepared using Al_2O_3/PtP_2-600 catalyst on GDL as cathode, Pt/C catalyst on GDL as anode, and Nafion 117 membrane. To prepare the cathode, a catalyst ink composed of Al_2O_3/PtP_2-600 dispersed in a water–ethanol mixture with ionomer (Nafion solution, 5 wt%) was sprayed on Teflon-treated or non-Teflon-treated GDL. Anode was prepared with commercial Pt/C (20 wt%) catalyst in the same manner as the cathode. The catalyst loading amount for cathode and anode is 0.8 mg_{PtP2} cm^{-2} and 0.3 mg_{Pt} cm^{-2}, respectively. A hot press (120 °C and 40 MPa for duration of 5 min) was used to press the components together with a Nafion 117 membrane. The MEA was then assembled in a single fuel cell consisting 4 cm^2 serpentine flow fields. Humidification of the MEA was performed for 60 min by flowing N_2 with 100% relative humidity at a cell temperature of 80 °C. The flow rates for H_2 and O_2 gases are 150 and 200 mL min^{-1}, respectively. The flow rate of external neutral water was controlled by a peristaltic pump. The pure water flow through the cathode chamber is beneficial for the removal of generated H_2O_2 molecules and to decrease the thermochemical decomposition and/or further electroreduction of H_2O_2. In the product recycling mode of operation, initially the system is run for 1 h run to accumulate 600 mL H_2O_2 solution which is then continuously cycled back through the system without any separation of the H_2O_2. All the conditions, such as mass loading, catalyst support, water flow rate, and operation temperature, were optimized for H_2O_2 production in the PEMFC. For quantitative analysis of H_2O_2 concentration, the interaction of the H_2O_2 with a modified iodate solution was monitored with the UV–vis spectrscopy method[44]. Briefly, solution A for the I_3^- method consisted of 33 g of KI, 1 g of NaOH, and 0.1 g of ammonium molybdate tetrahydrate diluted to 500 mL with water. The solution was stirred for ~10 min to dissolve the molybdate. Solution A was kept in the dark to inhibit the oxidation of I^-. Solution B, an aqueous buffer, contained 10 g of KHP per 500 mL. The pH was measured using a pH meter. Equal weights of A and B was subsequently mixed, followed by addition of the H_2O_2 solution. The absorbance of the resulting solution was measured at a maximum wavelength of 351 nm.

Based on the obtained concentration of flow H_2O_2 solution, the CE of H_2O_2 production can be calculated by the following equation:

$$CE\% = \frac{2FQC}{I} \times 100\%, \quad (4)$$

where F is Faraday's constant (96485 C mol^{-1}), Q is the water flow rate (L s^{-1}), C is the H_2O_2 concentration (mol L^{-1}), and I is the current (A). The corresponding H_2O_2 production rate can be expressed as following equation:

$$r(H_2O_2) = 3600QC/A, \quad (5)$$

where A is the MEA area (4 cm^2). Full details of experimental procedures can be found in the Supplementary Information.

Data availability

The data that support the findings of this study are available from the corresponding author upon reasonable request.

Received: 14 October 2019; Accepted: 6 July 2020;
Published online: 06 August 2020

References

1. Yi, Y., Wnag, L., Li, G. & Guo, H. A Review on Research progress in the direct synthesis of hydrogen peroxide from hydrogen and oxygen: noble-metal catalytic method, fuel-cell method and plasma method. *Catal. Sci. Technol.* **6**, 1593–11610 (2016).
2. Yang, S. et al. Toward the decentralized electrochemical production of H_2O_2: a focus on the catalysis. *ACS Catal.* **8**, 4064–4081 (2018).
3. Jiang, Y. et al. Selective electrochemical H_2O_2 production through two-electron oxygen electrochemistry. *Adv. Energy Mater.* **8**, 1801909 (2018).
4. Lu, Z. et al. High-efficiency oxygen reduction to hydorgen peroxide catalysed by oxidized carbon materials. *Nat. Catal.* **1**, 156–162 (2018).
5. Jirkovsky, J. S. et al. Single atom hot-spots at Au-Pd nanoalloys for eelectrocatalytic H_2O_2 production. *J. Am. Chem. Soc.* **133**, 19432–19441 (2011).
6. Siahrostami, S. et al. Enabling direct H_2O_2 production through rational electrocatalyst design. *Nat. Mater.* **12**, 1137–1143 (2013).
7. Zheng, Z., Ng, Y. H., Wang, D. W. & Amal, R. Epitaxial growth of Au-Pt-Ni nanorods for direct high selectivity H_2O_2 production. *Adv. Mater.* **28**, 9949–9955 (2016).
8. Greeley, J. et al. Alloys of platinum and early transition metals as oxygen reduction electrocatalysts. *Nat. Chem.* **1**, 552–556 (2009).
9. Mayrhofer, K. J. J., Hartl, K., Juhart, V. & Arenz, M. Degradation of carbon-supported Pt bimetallic nanoparticles by surface segregation. *J. Am. Chem. Soc.* **131**, 16348–16349 (2009).
10. Gray, J. E. et al. In vitro studies evaluating leaching of mercury from mine waste calcine using simulated human body fluids. *Environ. Sci. Technol.* **44**, 4782–4788 (2010).
11. Xiao, P., Chen, W. & Wang, X. A review of phosphide-based materials for electrocatalytic hydrogen evolution. *Adv. Energy Mater.* **5**, 1500985 (2015).
12. Yan, B. et al. Surface restructuring of nickel sulfide generates optimally coordinated active sites for oxygen reduction catalysis. *Joule* **1**, 600–612 (2017).
13. Li, H. et al. Earth-abundant iron diboride (FeB_2) nanoparticles as highly active bifunctional electrocatalysts for overall water splitting. *Adv. Energy Mater.* **7**, 1700513 (2017).
14. Sheng, Y. et al. Electrocatalytic production of H_2O_2 by selective oxygen reduction using earth-abundant cobalt pyrite (CoS_2). *ACS Catal.* **9**, 8433–8442 (2019).
15. Jirkovsky, J. S., Bjorling, A. & Ahlberg, E. Reduction of oxygen on dispersed nanocrystalline CoS_2. *J. Phys. Chem. C* **116**, 24436–24444 (2012).
16. Li, H. et al. Colloidal cobalt phosphide nanocrystals as trifunctional electrocatalysts for overall water splitting powered by a zinc–air battery. *Adv. Mater.* **30**, 1705796 (2018).
17. Shao, M., Peles, A. & Shoemaker, K. Electrocatalysis on platinum nanoparticles: particle size effect on oxygen reduction reaction activity. *Nano Lett.* **11**, 3714–3719 (2011).
18. Cao, M., Wu, D. & Cao, R. Recent advances in the stabilization of platinum electrocatalysts for fuel-cell reactions. *ChemCatChem* **6**, 26–45 (2013).
19. Zhang, Q., Lee, I., Ge, J., Zaera, F. & Yin, Y. Surface-protected etching of mesoporous oxide shells for the stabilization of metal nanocatalysts. *Adv. Funct. Mater.* **20**, 2201–2214 (2010).
20. Lu, J., Elam, J. W. & Stair, P. C. Synthesis and stabilization of supported metal catalysts by atomic layer deposition. *Acc. Chem. Res.* **46**, 1806–1815 (2013).
21. Lu, J. et al. Coking- and sintering-resistant palladium catalysts achieved through atomic layer deposition. *Science* **335**, 1205–1208 (2012).
22. Zhang, B. & Qin, Y. Interface tailoring of heterogeneous catalysts by atomic layer deposition. *ACS Catal.* **8**, 10064–10081 (2018).
23. Chen, Z. et al. Development of a reactor with carbon catalysts for modular-scale, low-cost electrochemical generation of H_2O_2. *React. Chem. Eng.* **2**, 239–245 (2017).
24. Yamanaka, I., Onizawa, T., Takenaka, S. & Otsuka, K. Direct and continuous production of hydorgen peroxide with 93% selectivity using a fuel-cell system. *Angew. Chem. Int. Ed.* **42**, 3653–3655 (2003).
25. Yamanaka, I. & Murayama, T. Neutral H_2O_2 synthesis by electrolysis of water and O_2. *Angew. Chem. Int. Ed.* **47**, 1900–1902 (2008).
26. Yamanaka, I., Tazawa, S., Murayama, T., Ichihashi, R. & Hanaizumi, N. Catalytic synthesis of neutral H_2O_2 solutions from O_2 and H_2 by a fuel cell reaction. *ChemSusChem* **1**, 988–990 (2008).
27. Li, W., Bonakdarpour, A., Gyenge, E. & Wilkinson, D. Drinking water purification by electrosynthesis of hydorgen peroxide in a power-producing PEM fuel cell. *ChemSusChem* **6**, 2137–2143 (2013).
28. Xu, J. et al. Carbon dioxide electroreduction into syngas boosted by a partially delocalized charge in molybdenum sulfide selenide alloy monolayers. *Angew. Chem. Int. Ed.* **56**, 9121–9125 (2017).
29. Becknell, N. et al. Atomic structure of Pt_3Ni nanoframe electrocatalysts by in situ X-ray absorption spectroscopy. *J. Am. Chem. Soc.* **137**, 15817–15824 (2015).
30. Li, X. & Gewirth, A. A. Oxygen electroreduction through a superoxide intermediate on Bi-modified Au surfaces. *J. Am. Chem. Soc.* **127**, 5252–5260 (2005).
31. Nayak, S., McPherson, I. J. & Vincent, K. A. Adsorbed intermediates in oxygen reduction on platinum nanoparticles observed by in situ IR spectroscopy. *Angew. Chem. Int. Ed.* **57**, 12855–12858 (2018).
32. Diaz-Morales, O., Calle-Vallejo, F., Munck, C. D. & Koper, M. T. M. Electrochemical water splitting by gold: evidence for an oxide decomposition mechanism. *Chem. Sci.* **4**, 2334–2343 (2013).
33. Nayak, S., Biedermann, P. U., Stratmann, M. & Erbe, A. A mechanistic study of the electrochemical oxygen reduction on the model semiconductor n-Ge(100) by ATR-IR and DFT. *Phys. Chem. Chem. Phys.* **15**, 5771–5781 (2013).
34. Jia, Q. et al. Roles of Mo surface dopants in enhancing the ORR performance of octahedral PtNi nanoparticles. *Nano Lett.* **18**, 798–804 (2018).
35. Cao, K., Cai, J., Liu, X. & Chen, R. Catalysts design and synthesis via selective atomic layer deposition. *J. Vac. Sci. Technol.* **36**, 010801 (2018).
36. Cao, K., Cai, J., Shan, B. & Chen, R. Surface functionalization on nanoparticles via atomic layer deposition. *Sci. Bull.* **65**, 678–688 (2020).
37. Zhang, J. et al. Origin of synergistic effects in bicomponent cobalt oxide-platinum catalysts for selective hydrogenation reaction. *Nat. Commum.* **10**, 4166 (2019).
38. Yang, N. et al. Rh-MnO interface sites formed by atomic layer deposition promote syngas conversion to higher oxygenates. *ACS Catal.* **7**, 5746–5757 (2017).
39. Singh, J. A. et al. Area-selective atomic layer deposition od metal oxides on noble metals through catalytic oxygen activation. *Chem. Mater.* **30**, 663–670 (2018).
40. Asundi, A. S. et al. Understanding structure-property relationships of MoO_3-promoted Rh catalysts for syngas conversion to alcohols. *J. Am. Chem. Soc.* **141**, 19655–19668 (2019).
41. Zalitis, C. M., Kramer, D. & Kucernak, A. R. Electrocatalytic performance of fuel cell reactions at low catalyst loading and high mass transport. *Phys. Chem. Chem. Phys.* **15**, 4329–4340 (2013).
42. Lee, M. & Huang, X. Development of a hydrophobic coating for the porous gas diffusion layer in a PEM-based electrochemical hydrogen pump to mitigate anode flooding. *Electrochem. Commun.* **100**, 39–42 (2019).
43. Allen, J. & Bard, L. R. F. *Electrochemical Methods: Fundamentals and Applications*. (Wiley, New York, NY, 2000).
44. Klassen, N. V., Marchington, D. & McGowan, H. C. E. H_2O_2 determination by the I_3^- method and by $KMnO_4$ titration. *Anal. Chem.* **66**, 2921–2925 (1994).

Acknowledgements

This work was financially supported by Wake Forest University, the Center for Functional Materials at Wake Forest University, National Science Foundation of Guangdong Province, China (2018A030313182), and Shenzhen Bureau of Science, Technology and Innovation Commission (JCYJ 20170811154527927). A portion of this research was conducted at the Center for Nanophase Materials Sciences, which is a DOE Office of Science User Facility. This work benefited from the Shanghai Synchrotron Radiation Facility (SSRF).

Author contributions

H.L. and P.W. synthesized the NCs. H.L., P.W., Z.H., C.L., S.A., and C.D. performed the physical characterizations. H.L., W.P., and X.M. performed all the electrochemical measurements. D.I. performed the DFT calculation. H.L., L.J., D.L.C., Y.Q., and S.M.G. designed the experiments and prepared the paper.

Competing interests

The authors declare no competing interests.

Additional information

Supplementary information is available for this paper at https://doi.org/10.1038/s41467-020-17584-9.

Correspondence and requests for materials should be addressed to Y.Q. or S.M.G.

Peer review information *Nature Communications* thanks Sungeun Yang and other, anonymous, reviewers for their contributions to the peer review of this work.

Reprints and permission information is available at http://www.nature.com/reprints

Publisher's note Springer Nature remains neutral with regard to jurisdictional claims in published maps and institutional affiliations.